Chinese Journal of
POLYMER SCIENCE

RESEARCH ARTICLE

https://doi.org/10.1007/s10118-026-3742-2
Chinese J. Polym. Sci.

Polyacrylonitrile (PAN)-derived Carbon Modification of Polysilazane Composite SiCNO/C as a High-performance Anode Material for Lithium-ion Batteries

Yi-Han Li, Yi-Wen Zhang, Jun-Hong Liu, Wen-Ze Xiao, Wen-Han Zang, Jing-Jiang Sun, Jian-Jiang He, Qing-Fu Wang*, and Wei Zhao*

Key Laboratory of Rubber-plastics, Ministry of Education, School of Polymer Science and Engineering, Qingdao University of Science and Technology, Qingdao 266042, China

Electronic Supplementary Information

Abstract Silicon-based anodes are promising candidates for next-generation lithium-ion owing to their high theoretical specific capacity. However, their practical application is limited by their severe volume expansion and poor electronic conductivity during cycling, which results in rapid capacity fading. To address these challenges, a novel polymer-derived ceramic (PDC) precursor, PSZ/PAN, was designed and synthesized by integrating polysilazane (PSZ) with polyacrylonitrile (PAN). The synthesis involved an initial free-radical polymerization of PSZ to form a crosslinked network, followed by *in situ* introduction and polymerization of acrylonitrile, yielding a PSZ/PAN hybrid with an interpenetrating network structure at the molecular level. Upon pyrolysis, the resulting SiCNO/C hybrid anode exhibited a high reversible specific capacity of 1050.1 mAh·g^{-1} at 500 mA·g^{-1} and excellent cycling stability, retaining 73.2% of its initial capacity after 600 cycles. This molecular-level interpenetrating design of polymer-derived ceramics provides a promising strategy for the development of high-performance anode materials for lithium-ion batteries.

Keywords Polysilazane; Acrylonitrile; Polymer-derived ceramic; Lithium-ion battery

Citation: Li, Y. H.; Zhang, Y. W.; Liu, J. H.; Xiao, W. Z.; Zang, W. H.; Sun, J. J.; He, J. J.; Wang, Q. F.; Zhao, W. Polyacrylonitrile (PAN)-derived carbon modification of polysilazane composite SiCNO/C as a high-performance anode material for lithium-ion batteries. *Chinese J. Polym. Sci.* https://doi.org/10.1007/s10118-026-3742-2

INTRODUCTION

The growing energy demands of portable electronics, electric vehicles, and grid-scale energy storage have driven intensive research into next-generation lithium-ion batteries (LIBs) with higher energy density, longer cycle life, and improved safety.[1] The anode material has become a central focus as a critical component governing overall battery performance. Although graphite anodes dominate the commercial market because of their low cost and stable cycling performance, their limited theoretical specific capacity (372 mAh·g^{-1}) is insufficient for emerging high-energy-density applications.[2] This limitation has prompted the exploration of alternative anode materials, including silicon, transition metal oxides, and various organic-inorganic composites.[3–6]

Among these candidates, silicon-based materials have attracted particular interest owing to their high theoretical capacity (about 4200 mAh·g^{-1}) and suitable operating voltage.[7] However, their practical implementation is hindered by two intrinsic drawbacks: massive volume changes (>300%) during lithiation/delithiation, which lead to electrode pulverization and rapid capacity decay, and low intrinsic electrical conductivity, which limits the rate performance.[8] To mitigate these issues, strategies such as nanostructuring,[9] carbon coating,[10] and dispersion within active or inactive matrices[11] have been explored. Nevertheless, these approaches often involve complex syntheses or fail to ensure long-term cycling stability, highlighting the need for novel materials with rationally designed architectures.

Polymer-derived ceramics (PDCs) have emerged as a promising class of materials owing to their unique structure and excellent electrochemical properties.[12,13] In particular, polysilazanes can be converted into silicon-carbon-nitrogen (SiCN) ceramics through high-temperature pyrolysis, yielding amorphous materials with chemical stability and tunable compositions. The free-carbon phase in SiCN provides abundant lithium storage sites, enabling high capacities. Under optimized conditions, polysilazane-derived SiCN anodes can achieve reversible capacities exceeding 500 mAh·g^{-1}, substantially higher than those of graphite.[14]

Despite their potential, the direct application of polysi-

* Corresponding authors, E-mail: wangqf@qust.edu.cn (Q.F.W.)
E-mail: zwqust@qust.edu.cn (W.Z.)
Received May 13, 2026; Accepted May 30, 2026; Published online July 24, 2026

lazane-derived SiCN ceramics remains a challenge. Pure SiCN suffers from low electronic conductivity and significant volume variation during lithiation/delithiation, leading to poor cycling stability. To address these limitations, polysilazanes have been combined with carbon materials and conductive polymers to enhance their electrochemical performance.[15–17] Among these, polyacrylonitrile (PAN), a widely used carbon precursor, can generate a conductive carbon network upon pyrolysis, making it an attractive candidate for constructing composite anodes.[18] Previous studies have employed electrospinning to fabricate polysilazane/PAN composite fibers, which can be converted into SiCN/C materials with improved electrochemical properties after pyrolysis. However, these approaches are typically based on physical blending, resulting in limited interfacial interactions between the polysilazane and PAN. Consequently, issues such as inhomogeneous phase distribution and weak interfacial adhesion may arise, ultimately restricting overall electrochemical performance.

In this study, we report a straightforward and effective strategy for the construction of a novel polymer-derived ceramic precursor, polysilazane-acrylonitrile (PSZ/PAN). The synthesis involves a two-step sequential polymerization. First, polysilazane undergoes free-radical polymerization to form a crosslinked network, followed by *in situ* polymerization of acrylonitrile within the PSZ matrix. This approach ensures intimate molecular-level mixing and strong interfacial interactions between the ceramic framework (PSZ) and the carbon source (PAN). Upon pyrolysis, the resulting SiCNO/C composite combines the advantages of both components, providing a mechanically stable scaffold that mitigates volume expansion during cycling, whereas the embedded PAN-derived carbon forms a continuous conductive pathway and contributes additional electrochemically active sites for lithium storage. As an anode for LIBs, the SiCNO/C electrode demonstrated high reversible capacity, excellent rate capability, and long-term cycling stability. These results highlight the molecular-level design of polymer-derived ceramics as a promising strategy for the next-generation high-performance anode materials.

EXPERIMENTAL

Material

Dichloromethylsilane (98%), dichloromethylvinylsilane (97%), and 3-aminopropyltriethoxysilane (99%) were purchased from Sigma-Aldrich (Shanghai, China). *n*-Hexane and anhydrous ethanol were obtained from Sinopharm Chemical Reagent (Shanghai, China). Azodiisobutyronitrile (AIBN) and 1,4-dioxane were supplied by Sun Chemical Technology (Shanghai, China). Acrylonitrile was purchased from Adamas (Shanghai, China). All the chemicals were used as received without further purification.

Synthesis of Organopolysilazane Oligomer OPSZ

In a 2 L three-necked round-bottom flask equipped with a mechanical stirrer, thermometer, and dry ice/isopropanol condenser, 600 mL of *n*-hexane was added. Methylhydrodichlorosilane (0.24 mol), methylvinyldichlorosilane (0.06 mol), and 3-aminopropyltriethoxysilane (0.6 mol) were added sequentially under stirring. The reaction mixture was cooled in an ice bath and maintained at approximately 20 °C for 2 h. Ammonia gas was then slowly introduced over 2 h, and the temperature at 20 °C by adjusting the gas flow rate. After the completion of ammonolysis, the resulting ammonium chloride precipitate was removed by filtration, and the filter cake was washed three times with 100 mL of *n*-hexane. The combined filtrate was subjected to vacuum distillation at 40 °C to remove residual ammonia and solvent, yielding the liquid organopolysilazane oligomer (OPSZ).

Synthesis of PSZ/PAN

The synthesis of PSZ/PAN was performed as follows: 400 mg of organic polysilazane oligomer OPSZ (0.8 mmol) was dissolved in 40 mL of 1,4-dioxane in a reaction tube. Azobisisobutyronitrile (0.008 mmol) was added to facilitate complete dissolution. To remove oxygen, the system underwent three freeze–pump–thaw cycles, after which the reaction was conducted at 70 °C for 8 h under an argon atmosphere. Upon completion of the initial reaction, acrylonitrile (AN, 4 mmol) and AIBN (0.04 mmol) were added to the reaction mixture. The system was again deoxygenated *via* a freeze-pump-thaw cycle, followed by the injection of the monomer solution under argon. The second polymerization was carried out at 70 °C for 8 h. After the reaction, the mixture was centrifuged at 8000 r·min^{-1} for 10 min to remove excess solvent and unreacted monomers. The resulting precipitate was resuspended in anhydrous ethanol, ultrasonicated for 10 min, and washed three times by repeated centrifugation. Finally, the purified PSZ/PAN product was vacuum-dried at 80 °C for 12 h to obtain the desired PSZ/PAN hybrid material.

Preparation of SiCNO/C and SiCNO

The PSZ/PAN precursor obtained was placed in a tube furnace and pyrolyzed under a nitrogen atmosphere. The temperature was increased to 1000 °C at a rate of 10 °C·min^{-1}, maintained at 1000 °C for 3 h, and then allowed to cool naturally to room temperature, yielding a SiCNO/C hybrid material. For comparison, the control sample, consisting of an organic polysilazane oligomer (OPSZ), was cured in a vacuum oven at 80 °C for 24 h. The cured solid was coarsely ground using an agate mortar and milled at 300 r·min^{-1} for 6 h to obtain a uniform fine powder. This powder was then pyrolyzed under nitrogen under the same conditions—heated to 1000 °C at 10 °C·min^{-1}, held for 3 h, and cooled naturallyto produce the pure SiCNO ceramic material.

Preparation of Half-cell

The SiCNO/C and SiCNO materials obtained by pyrolysis were used as the active materials for the preparation of the working electrodes. Sodium carboxymethyl cellulose (CMC) and styrene-butadiene rubber (SBR) emulsions served as binders, while conductive carbon black (Super P) was used as the conductive additive. The components were mixed at a mass ratio of active material: Super P:CMC:SBR= 6:2:1.2:0.8. An appropriate amount of deionized water was added as the dispersion medium and the mixture was thoroughly stirred to form a uniform electrode slurry. The slurry was evenly coated onto copper foil current collectors by using a scraper and allowed to rest at room temperature for 2 h. The coated electrodes were then dried in a vacuum oven at 80 °C for 12 h to remove residual moisture. After drying, electrode sheets were rolled, cut, and stored for subsequent use.

https://doi.org/10.1007/s10118-026-3742-2

The electrodes were assembled into 2032-type coin cells in an argon-filled glove box (H_2O and O_2 < 0.01 cm^3/m^3), using lithium metal (16 mm diameter, 0.6 mm thickness) as the counter electrode. The electrolyte consisted of 1 mol·L^{-1} LiPF6 dissolved in a 1:1 (*V*:*V*) mixture of dimethyl carbonate and ethylene carbonate. A Celgard 2500 separator (25 μm thick, 18 mm diameter) was placed between the electrodes. After assembly, the cells were sealed, allowed to stand at room temperature for 12 h to ensure thorough electrolyte penetration, and subjected to electrochemical testing.

Characterization

The chemical structure of OPSZ was analyzed using ^{1}H-NMR spectroscopy. The functional groups were characterized using Fourier-transform infrared spectroscopy (FTIR, BRUKER VERTEX 70). Prior to FTIR analysis, the OPSZ sample was centrifuged using a high-speed desktop centrifuge (TG16-WS) to remove impurities. The microstructures of the samples were examined by scanning electron microscopy (SEM, JSM7500F), and the crystal structure was determined by X-ray diffraction (XRD, Rigaku D/MAX/2500 PC) using Cu Kα radiation (λ=0.15418 nm) over the 2θ range of 5°–90°. The molecular composition and structure were further analyzed by confocal micro-Raman spectroscopy (Raman, INVIA), whereas the surface elemental composition and chemical states were characterized by X-ray photoelectron spectroscopy (XPS, Thermo Fisher ESCALAB XI+). Thermal stability and decomposition behavior were evaluated by thermogravimetric analysis (TGA, TG209F1-JRIS) in air at a heating rate of 20 °C/min from room temperature to 800 °C. The electrochemical performance of the assembled button cells was measured using a LAND CT3002A battery test system (Wuhan Landian Electronics Co., Ltd.). Galvanostatic charge-discharge tests were conducted at room temperature within a voltage window of 0.01–2.0 V (versus Li^+/Li). All the specific capacities were calculated based on the mass of the active material (SiCNO/C hybrid or pure SiCNO).

RESULTS AND DISCUSSION

Traditional emulsion and template methods for the preparation of polysiloxane-based nanomaterials often suffer from severe particle agglomeration and poor dispersion. In this study, a molecular design approach was employed to construct PSZ/PAN hybrid precursors *via* free-radical polymerization combined with an *in situ* acrylonitrile injection strategy, followed by pyrolysis to obtain SiCNO/C composite anode materials. The abundant reactive groups (Si—H, Si—N) in the PSZ facilitate hybridization, while the *in situ* polymerization of PAN enables uniform interpenetration of the two phases at the molecular level, effectively preventing macroscopic phase separation. The resulting SiCNO/C hybrid exhibits several advantages: (i) the PAN-derived carbon network forms a continuous conductive pathway and buffers volume expansion during cycling; and (ii) nitrogen-doped sites and the amorphous SiCNO matrix provide abundant lithium storage active centers. This simple and controllable molecular engineering strategy—polymerization first, injection later, followed by pyrolysis—offers a new approach to overcoming the nanoparticle agglomeration common in traditional methods. The prepared materials demonstrated promising potential as anodes for lithium-ion batteries (Scheme 1).

Synthesis and Characterization of Organopolysilazane Oligomers (OPSZ)

The organic polysilazane oligomer (OPSZ) was synthesized *via* the aminolysis of methylhydrodichlorosilane, methylvinyldichlorosilane, and 3-aminopropyltriethoxysilane. The chemical structure of the product was confirmed by ^{1}H-NMR and Fourier transform infrared spectroscopy (FTIR). In the ^{1}H-NMR spectrum (Fig. S1 in the electronic supplementary information, ESI), signals corresponding to Si—CH=CH_2 (6.12–5.77 ppm), Si—H (about 4.66 ppm), and Si—CH_3 (0.34–0.07 ppm) were clearly observed, consistent with the FTIR

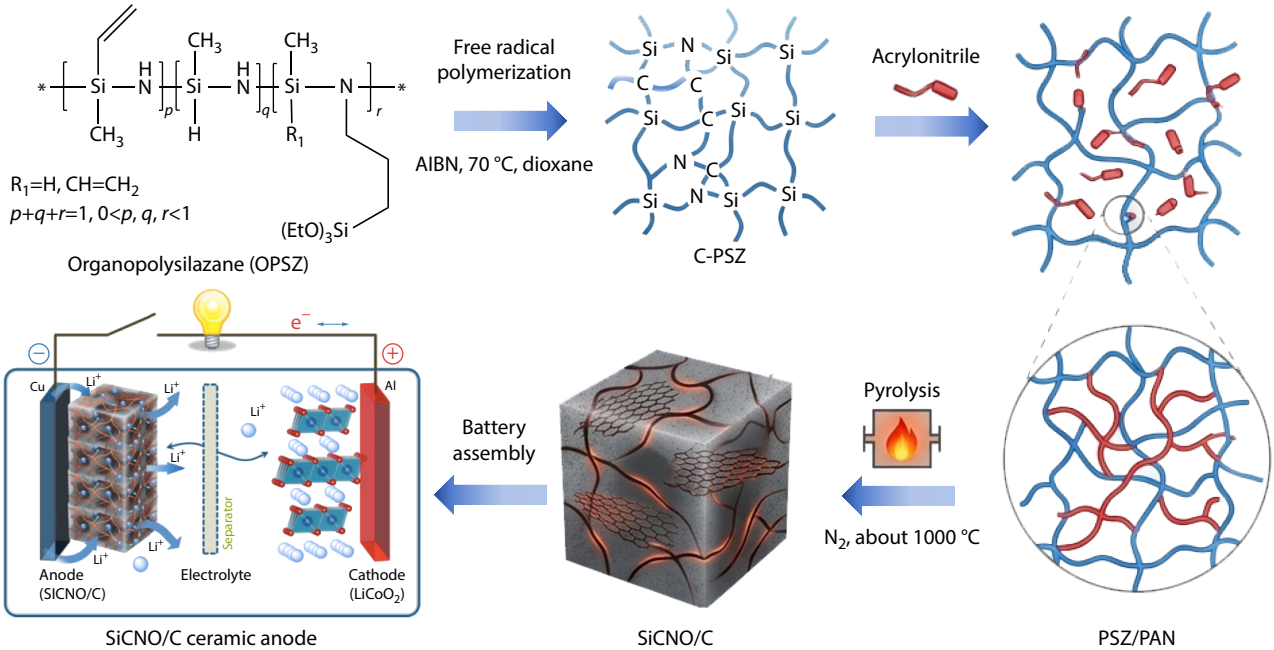

Scheme 1 Synthesis of SiCNO/C and its application as a ceramic anode in lithium-ion batteries.

results. FTIR analysis (Fig. S2 in ESI) further verified the chemical structure of the OPSZ. The absorption bands at 3053 and 2974 cm^{-1} were assigned to C—H stretching of the vinyl siloxane group (Si—CH=CH_2), and the C=C stretching vibration appeared at about 1590 cm^{-1}. The band at 2140 cm^{-1} corresponded to the Si—H stretching vibration. The presence of the Si—NH—Si unit was confirmed by N—H stretching at 3394 cm^{-1} and Si—N vibration at 953 cm^{-1}. Additionally, the Si—CH_3 group exhibited a characteristic absorption at 1251 cm^{-1}, accompanied by C—H stretching at 2931 and 2885 cm^{-1}.[19]

Characterization of Morphology, Structure and Composition of PSZ/PAN Hybrid Materials

The preparation of PSZ/PAN hybrid materials was performed in two steps. First, OPSZ underwent free radical polymerization to form a cross-linked polysilazane network (denoted as C-PSZ). Next, acrylonitrile (AN) was added for copolymerization or *in situ* polymerization to yield a polysilazane-polyacrylonitrile hybrid precursor (PSZ/PAN). The precursor was subsequently pyrolyzed at 1000 °C under a nitrogen atmosphere to produce a SiCNO/C composite ceramic material.

The FTIR analysis revealed the reaction mechanism. As shown in Fig. S2 (in ESI), the C—H stretching vibration peaks (2974 cm^{-1} and 3053 cm^{-1}) in the Si—CH=CH_2 groups and the C=C stretching vibration peak (1598 cm^{-1}) in C-PSZ exhibited attenuation, indicating free radical polymerization. The disappearance of N—H and Si—H bonds suggests dehydrogenation reactions between the Si—H and N—H groups. Fig.1 illustrates the reaction mechanism between C-PSZ and acrylonitrile. In the PSZ/PAN system, a C≡N stretching vibration peak appeared at 2270 cm^{-1}, while the C—H bands (2974 and 3053 cm^{-1}) and C=C bands (1598 cm^{-1}) on Si—CH=CH_2 were nearly absent, confirming the successful acrylonitrile incorporation. After 1000 °C pyrolysis, the corresponding peaks of —Si—CH_3 (1267 cm^{-1}) and —CH_2— (2927 cm^{-1}) disappeared, while Si—O (1076 cm^{-1}) and Si—C (821 cm^{-1}) remained, confirming the precursor's conversion into ceramic material.[20]

Fig. 2(a) shows the XRD spectrum of the SiCNO/C composite, exhibiting distinct broad diffraction peaks around 23° and 43°, indicating that the SiCNO ceramic exhibits an amorphous structure with SiCNO predominantly in an amorphous/low-crystallinity state.[21] Fig. 2(b) shows the Raman spectrum of SiCNO/C, exhibiting the characteristic D (about 1350 cm^{-1}) and G (about 1580 cm^{-1}) bands of carbon materials. The relatively low I_D/I_G ratio suggests an increased degree of graphitization, which can be attributed to the formation of graphitic domains during carbonization of PAN, thereby enhancing the electrical conductivity of the composite. The presence of a pronounced D band indicated that the SiCNO/C structure retained abundant carbon defects. These defects, together with heteroatom doping sites, provide additional active sites for lithium storage and help buffer volume changes during cycling, ultimately contributing to the improved capacity and cycling stability.[22]

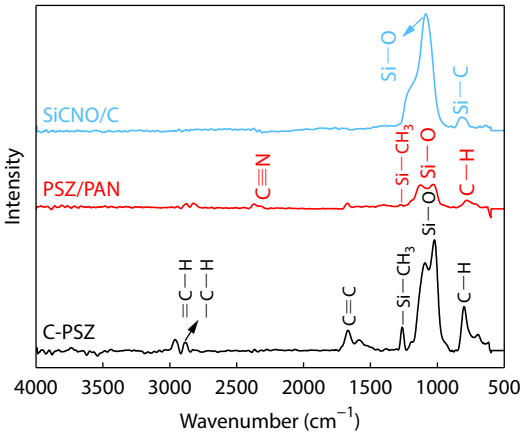

Fig. 1 FTIR spectra of C-PSZ, PSZ/PAN and SiCNO/C.

Figs. 3(a) and 3(b) show the EDS surface mapping of PSZ and PSZ/PAN, respectively, and the corresponding elemental compositions are summarized in Table S1 (in ESI). Compared with PSZ, PSZ/PAN exhibited a significant increase in the carbon signal intensity and carbon content, directly confirming the successful incorporation of polyacrylonitrile. Concurrently, the relative silicon and oxygen contents decreased, reflecting the "dilution" effect of acrylonitrile-derived organic chains on the polysilazane framework. This elemental composition adjustment provides a favorable basis for subsequent pyrolysis to produce SiCNO-based anode materials with high carbon content and conductivity, which is expected to enhance the electrochemical performance in lithium-ion batteries. Fig. S3 (in ESI) shows the thermogravimetric analysis results of

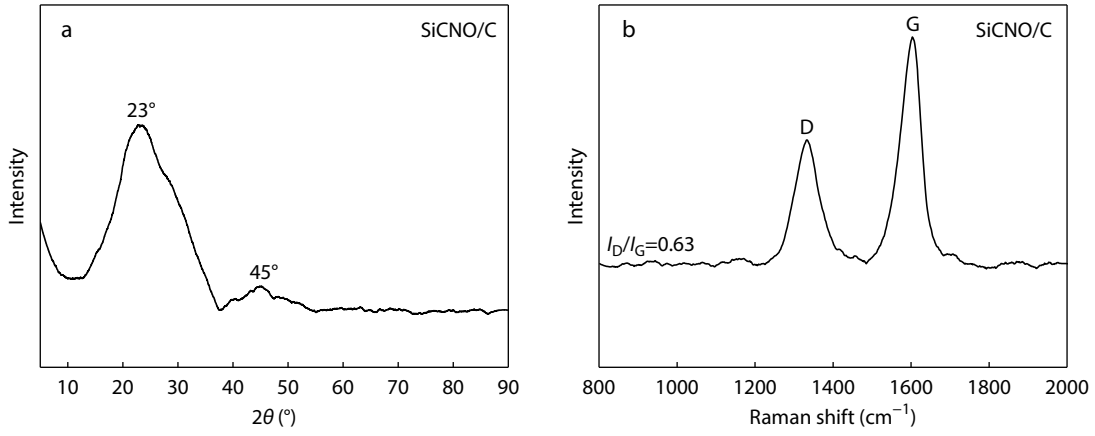

Fig. 2 (a) XRD pattern of SiCNO/C; (b) Raman scattering spectrum of SiCNO/C.

https://doi.org/10.1007/s10118-026-3742-2

PSZ and PSZ/PAN in air. The residual weight of PSZ from room temperature to 800 °C was 51.81%, whereas PSZ/PAN retained only 36.02%, indicating a lower ceramic yield because of the more easily oxidized and decomposable organic polyacrylonitrile segments, further confirming their successful incorporation. Furthermore, the effect of the OPSZ:AN molar ratio on the thermal decomposition behavior of the precursors was investigated, as shown in Fig. S4 (in ESI). With an increase in AN content, the ceramic yield at 800 °C progressively declined from 61.77% to 40.14%. This decrease was attributed to the more pronounced decomposition of the organic species originating from PAN. This result confirms that the ratio of OPSZ to AN can effectively regulate the carbon content and ceramic yield of the resulting SiCNO/C composite, thereby providing a basis for compositional optimization.

To confirm that the reaction between PSZ and AN proceeded *via* copolymerization rather than simple physical blending, the resulting PSZ/PAN product was subjected to solubility and ^{1}H-NMR analyses using *N*,*N*-dimethylformamide (DMF) as the testing solvent. DMF is an excellent solvent for PAN; thus, in a physical blend of PSZ and PAN, DMF selectively dissolves the PAN component to form a homogeneous solution. In contrast, successful copolymerization leads to chemical bonding between PSZ and PAN, altering the molecular structure and solubility of the product, rendering it insoluble in DMF. Solubility tests (Fig. S5 in ESI) showed that the PSZ/PAN samples remained insoluble in DMF and maintained a heterogeneous state, which preliminarily supported the formation of a copolymer structure. Further ^{1}H nuclear magnetic resonance characterization of the DMF supernatant from sample S5 (Fig. S6 in ESI) revealed only signals corresponding to DMF-derived CHO (7.76 ppm) and methyl groups (2.49–2.87 ppm), with no characteristic signals associated with the PAN or PSZ components, confirming the absence of soluble polymers in the DMF phase. Collectively, these results rule out the possibility of physical blending and conclusively demonstrate that copolymerization occurs between PSZ and acrylonitrile, yielding a PSZ/PAN copolymer that remains completely insoluble in DMF.

The microstructures of the PSZ/PAN precursor and the resulting pyrolyzed SiCNO/C ceramic are shown in Figs. 4(a) and 4(b), respectively. The PSZ/PAN precursor exhibited a loose, nanoscale aggregate structure comprising adherent particles that formed porous fluffy clusters. Following pyrolysis at 1000 °C, these nanoclusters underwent sintering into dense submicron ceramic particles, which coalesced to form a continuous ceramic network. This densification was expected to enhance the mechanical integrity and electrochemical cycling stability of the material.

Fig. 5 shows the results of X-ray photoelectron spectroscopy (XPS) to investigate the changes in the surface chemical bonding states before and after pyrolysis. In the Si2p spectrum, the main peak shifted from 102.5 eV in PSZ/PAN to 101.9 eV in SiCNO/C, indicating a significant change in the silicon chemical environment due to Si—O bond cleavage and the formation of new Si—C bonds. The O 1s spectrum showed a marked reduction in the intensity of Si—O peaks at 531.4 and 531.8 eV after pyrolysis, further confirming deoxygenation. The C 1s spectrum of SiCNO/C exhibited peaks at 283.5 eV and 284.8 eV, corresponding to C—Si and C—C/C=C bonds, respectively, along with a C—O/C—N component at 286.8 eV, confirming nitrogen incorporation into the carbon network. Notably, the C=C bonds present in the OPSZ were consumed during polymerization, and the in-

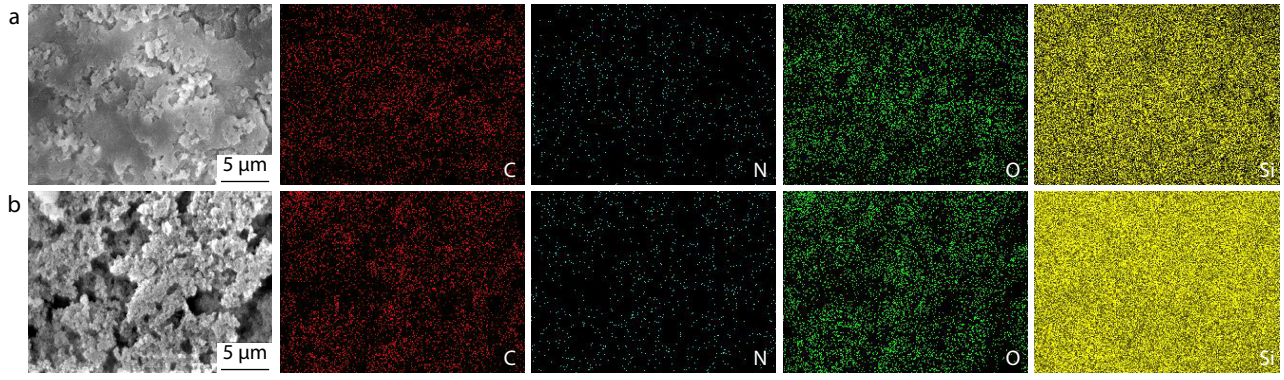

Fig. 3 (a) SEM image and corresponding EDS spectra of C, O, N and Si in PSZ; (b) SEM image and corresponding EDS spectra of C, O, N and Si in PSZ/PAN.

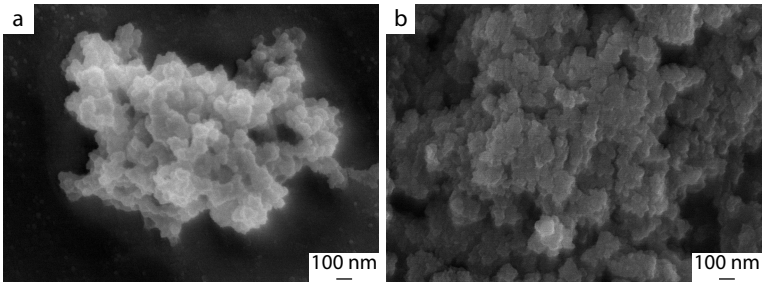

Fig. 4 SEM images of (a) PSZ/PAN and (b) SiCNO/C.

https://doi.org/10.1007/s10118-026-3742-2

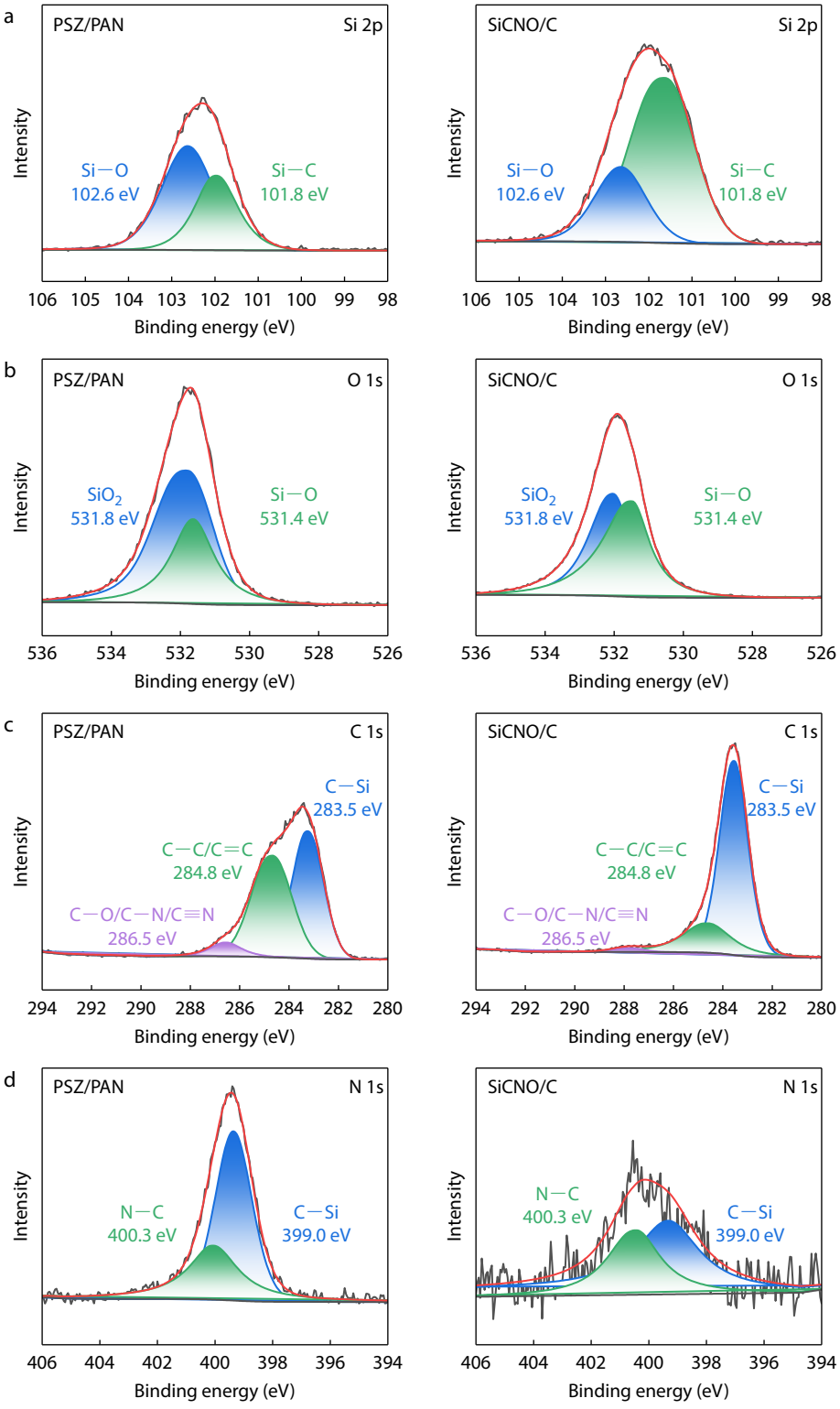

Fig. 5 High-resolution XPS spectra of PSZ/PAN and SiCNO/C in (a) Si 2p, (b) O 1s, (c) C 1s, (d) N 1s.

creased intensity of the C—Si peak after pyrolysis indicates extensive Si—C formation. The N 1s spectrum displayed a dominant peak at 399.4 eV, which could be further deconvoluted into N—Si (398.8 eV) and N—C (400.4 eV) components, confirming that nitrogen is covalently bonded to both silicon and carbon. Collectively, these results demonstrate that pyrolysis transforms the PSZ/PAN precursor into a SiCNO/C ceramic with a chemically bonded Si—C—N network and nitrogen-doped carbon, which is consistent with the observed structural and functional properties.

In addition to structural and compositional analyses, the specific surface area and pore structure characteristics of SiCNO and SiCNO/C were evaluated using N_2 adsorption-desorption measurements. As shown in Fig. S7 and Table S2 (in ESI), SiCNO exhibited an extremely low nitrogen uptake on its adsorption isotherm, corresponding to a BET specific surface area of only 0.18 $m^2 \cdot g^{-1}$. This indicates that SiCNOs possess a dense, nonporous ceramic structure. In contrast, the BET specific surface area of SiCNO/C significantly increases to 14.77 $m^2 \cdot g^{-1}$, confirming that the incorporation of PAN-derived carbon effectively enhances the availability of surface sites. Notably, neither sample displayed hysteresis loops in its isotherms, suggesting the absence of open mesopores (2–50 nm) in either material. Consequently, the SiCNO/C composite exhibited a unique structural configuration, with a relatively high specific surface area arising primarily from external surface exposure and/or narrow micropores, without the presence of mesoporous channels that typically promote electrolyte decomposition and irreversible lithium consumption. This combination of mesopore-free yet surface-rich architecture is particularly advantageous for lithium-ion battery anodes, as it achieves an optimal balance between providing sufficient active sites and suppressing adverse side reactions.[23]

Electrochemical Performances of SiCNO/C as Anode for Lithium-ion Batteries

The lithium-ion insertion/deintercalation behavior of the SiCNO and SiCNO/C composite materials was investigated using cyclic voltammetry (CV). Fig. 6 shows the CV curves of the first five cycles of both electrodes at a scan rate of 0.1 $mV \cdot s^{-1}$ within a voltage range of 0–2.5 V. For the SiCNO/C electrode, a broad reduction peak appears at approximately 0.7 V during the initial scan, which gradually weakens and eventually disappears in subsequent cycles. This behavior was attributed to the irreversible formation and stabilization of the solid electrolyte interfacial (SEI) film. The reduction peak observed in the 1.0–1.75 V range corresponds to the formation of irreversible products such as lithium silicate (Li_4SiO_4, $Li_2Si_2O_5$) and Li_2O.[24] In subsequent cycles, a new reduction peak emerges near 0.2 V, indicative of lithium alloying with amorphous silicon, while a broad oxidation peak appears around 0.6 V, associated with the deintercalation process of silicon-lithium alloys.[25] Furthermore, the SiCNO/C composite electrode exhibited a higher response current intensity, reflecting its superior electrochemical activity. In contrast, the pure SiCNO electrode exhibited no distinct redox peaks under identical testing conditions and maintained consistently low current responses, suggesting sluggish lithiation/delithiation kinetics, limited reversible capacity, and poor lithium storage performance. These results demonstrate that the SiCNO/C composites possess a significantly enhanced lithium-ion storage capability compared to pure SiCNO.

The lithium-ion diffusion kinetics of the SiCNO/C composite electrode were evaluated using the constant-current intermittent titration technique (GITT). Fig. S8(a) (in ESI) shows the voltage-time curves during the discharge/charge cycles. During discharge, the voltage decreases from 3.0 V to 0 V, with a distinct voltage plateau observed in the 0.01–0.3 V range of the silicon-lithium alloyation reaction.[26] The initial charging voltage of 0.5 V indicates the presence of a delamination lag.[27] Fig. S8(b) (in ESI) shows the $\lg(D_{Li+})$-voltage curve. In the early discharge phase (3.0–1.0 V), $\lg(D_{Li+})$ rapidly declines from −9.4 to −10.5; it reaches a minimum of approximately −11.5 ($D_{Li+} = 3\times10^{-12}$ $cm^2 \cdot s^{-1}$) in the 0.01–0.3 V alloyation region, reflecting the high diffusion barrier for lithium ions within the amorphous SiCNO matrix. During charging, $\lg(D_{Li+})$ slowly increases from 0.5 V to 1.5 V, followed by an inflection point around 2.0 V, which is attributed to the rapid release of interfacial charge. The GITT results demonstrate that despite the inherently high diffusion barrier of the SiCNO matrix, the incorporated carbon structure significantly enhanced the high-rate performance of the electrode by shortening the ion migration path within the low-diffusion region.[28,29]

Fig. 7 comprehensively evaluates the electrochemical performance of the SiCNO/C composite in comparison with that of the pristine SiCNO. The initial galvanostatic charge-discharge profiles (Fig. 7a) at 100 $mA \cdot g^{-1}$ reveal that the SiCNO/C electrode delivers a higher discharge capacity (2749.0 $mAh \cdot g^{-1}$) and charge capacity (1950.0 $mAh \cdot g^{-1}$), corresponding to an initial Coulombic efficiency (ICE) of 71.0%, which is markedly improved relative to SiCNO (59.0%). This improvement indicates a reduced irreversible lithium consumption and enhanced initial reversibility, which can be attributed to the optimized electrode/electrolyte interface. The carbon coating effectively suppressed the direct contact between

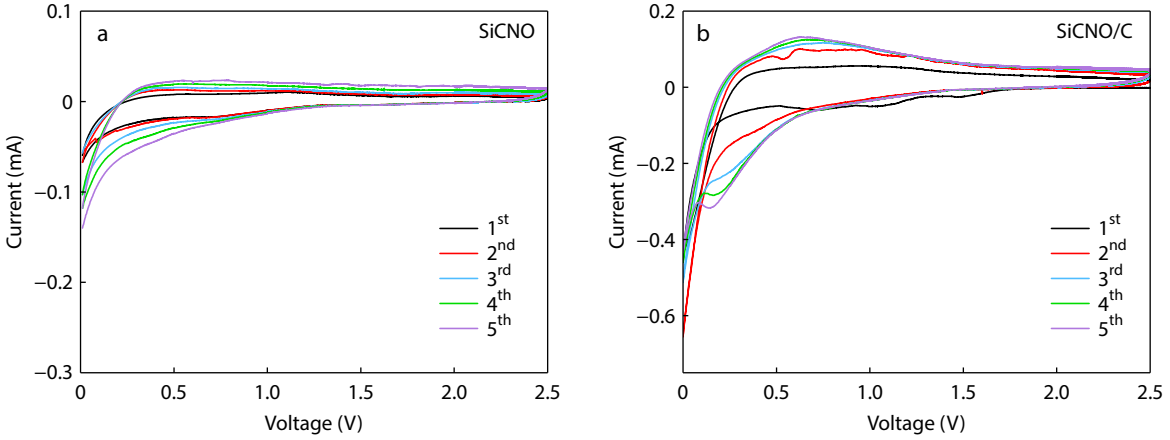

Fig. 6 Cyclic voltammetry curves of (a) SiCNO and (b) SiCNO/C.

https://doi.org/10.1007/s10118-026-3742-2

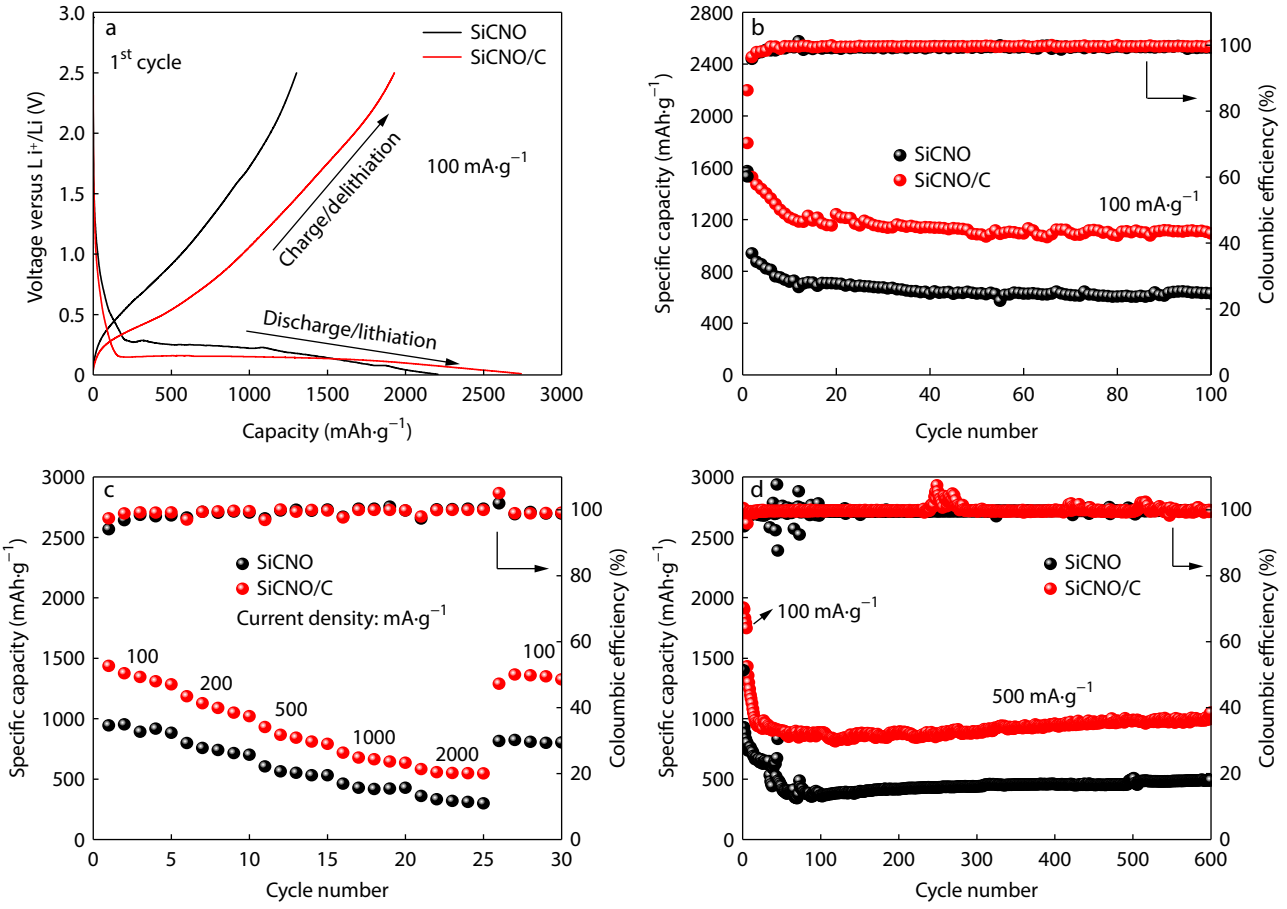

Fig. 7 (a) First cycle voltage profiles of SiCNO/C and SiCNO; (b) Cycling performance and Coulombic efficiency of SiCNO/C and SiCNO at a current density of 100 mA·g^{-1}; (c) Rate performance of SiCNO/C and SiCNO; (d) Long-cycle performance of SiCNO/C and SiCNO at a current density of 500 mA·g^{-1}.

SiCNO and the electrolyte, thereby mitigating excessive electrolyte decomposition and promoting the formation of thinner and more stable SEI films. Meanwhile, the carbon matrix provides mechanical flexibility to accommodate volume expansion during lithiation, prevent particle pulverization, and maintain electrode integrity.[30]

Fig. 7(b) compares the cycling performance and Coulombic efficiency of the SiCNO/C electrodes with those of pure SiCNO electrodes at a current density of 100 mA·g^{-1}. During the initial 20 cycles, both electrodes exhibited rapid irreversible capacity decay caused by the intense formation and reorganization of SEI films, structural pulverization induced by volume effects of the active material, and loss of electrical contact.[31] As cycling progressed, the SEI films gradually stabilized, and the material structures along with the conductive networks underwent adaptive restructuring, leading to a significant reduction in irreversible lithium consumption, slower capacity decay, and stabilized capacity retention. Throughout the cycling process, the SiCNO/C electrodes consistently delivered higher charge-discharge specific capacities and Coulombic efficiencies compared to the pure SiCNO electrodes. After 100 cycles, the SiCNO/C electrodes maintained a discharge specific capacity of 1091.6 mAh·g^{-1}, Coulombic efficiency of 99.8%, and capacity retention rate of 50.0%. These results indicate that carbon coating modification not only endows SiCNO/C electrodes with highly reversible electrochemical behavior during lithiation/delithiation processes, but also promotes robust SEI film formation, effectively suppressing electrolyte side reactions with the electrolyte. In contrast, under identical testing conditions, the pure SiCNO electrodes exhibited pronounced capacity decay, retaining only 628.5 mAh·g^{-1} with a capacity retention rate of only 39.9%.

The rate performance (Fig. 7c) further demonstrates the kinetic advantages of SiCNO/C. The composite electrode consistently delivered higher capacities than SiCNO across all current densities. Notably, when the current density was returned to 100 mA·g^{-1}, the capacity nearly recovered to its initial level, indicating excellent structural robustness and reversibility under high-rate cycling conditions.

Fig. 7(d) compares the long-term cycling performance and Coulombic efficiency of the SiCNO/C electrodes with those of the pristine SiCNO electrodes. After the initial three activation cycles at a current density of 100 mA·g^{-1}, both electrodes were subjected to 600 cycling tests at a higher current density of 500 mA·g^{-1}. The results demonstrated that the SiCNO/C electrodes exhibited excellent long-term stability, maintaining a high reversible specific capacity of 1050.1 mAh·g^{-1} after 600 cycles, corresponding to a capacity retention rate of 73.2%. Although both electrodes maintained a relatively sta-

ble Coulombic efficiency throughout cycling, the SiCNO/C electrodes not only delivered significantly higher specific capacities but also showed superior initial reversibility. Their Coulombic efficiency remained at around 99%, indicating highly reversible electrochemical reactions and robust electrode/electrolyte interface stability. Notably, a gradual increase in the specific capacity was observed after approximately 200 cycles, which can be attributed to the electrochemical activation of the electrode material. Structural rearrangements induced by prolonged cycling, along with progressive electrolyte penetration, continuously expose new lithium storage sites such as defects and interfaces. In SiCNO/C electrodes, the additional free carbon phase introduces a higher density of edge/heteroatom defects as well as ceramic/carbon interfaces, thereby enhancing the activation effect. Simultaneously, the flexible carbon network maintained excellent conductivity and structural integrity, facilitating the reversible contribution of surface adsorption and interfacial lithium storage. Consequently, the SiCNO/C electrodes exhibited a more pronounced capacity increase than their pristine counterparts.[15,32]

The superior performance of the SiCNO/C originates from its rationally engineered composite structure (Fig. 8). The PAN-derived carbon layer serves as a multifunctional component, simultaneously enhancing the electrical conductivity, facilitating lithium-ion transport, and buffering volume variations during repeated lithiation/delithiation. In addition, nitrogen doping and defect-rich carbon domains provide abundant active sites for Li storage. Collectively, these synergistic effects stabilize the electrode/electrolyte interface, suppress structural degradation, and enable the concurrent realization of a high capacity, excellent rate capability, and long-term cycling stability.

Electrochemical impedance spectroscopy (EIS) further elucidated the effect of the PAN-derived carbon modification on the reaction kinetics (Fig. 9). As shown in Fig. 9(a), the charge transfer resistance (R_{ct}) of SiCNO/C before cycling is 117.1 Ω, which is significantly lower than that of pristine SiCNO (137.5 Ω), indicating that the incorporation of PAN-derived carbon effectively reduces the interfacial charge transfer barrier.[33] This improvement facilitates faster electron transport and enhances the lithium-ion kinetics. The impedance spectra before and after cycling were fitted using the equivalent circuit model (Fig. 9b); the fitted parameters are summarized in Table S3. As shown in Figs. 9(c) and 9(d), the R_{ct} values decreased after the initial cycle owing to electrode activation,[34] remained relatively stable over 50 cycles, and slightly increased after prolonged cycling (100 cycles), which can be attributed to gradual structural degradation and accumulation of interfacial by-products. Notably, the SiCNO/C electrode consistently exhibited a lower R_{ct} than SiCNO throughout cycling, reflecting the formation of a continuous three-dimensional conductive network derived from PAN carbonization.

The lithium-ion diffusion coefficient (D_{Li+}) was calculated based on the Warburg impedance (Fig. S9 in ESI) according to Eq. (1):

$$D_{Li^+} = \frac{R^2T^2}{2A^2n^4F^4C^2\sigma^2} \quad (1)$$

where R is the ideal gas constant, T is the absolute temperature, A is the electrode surface area, n is the number of electrons transferred per mole of the substance, F is the Faraday constant, C is the molar concentration of Li^+ in the electrode material, and σ is the Warburg impedance coefficient.

The calculated D_{Li+} value for SiCNO/C is 7.2×10^{-15} $cm^2 \cdot s^{-1}$, which is significantly higher than that of SiCNO (2.3×10^{-15}

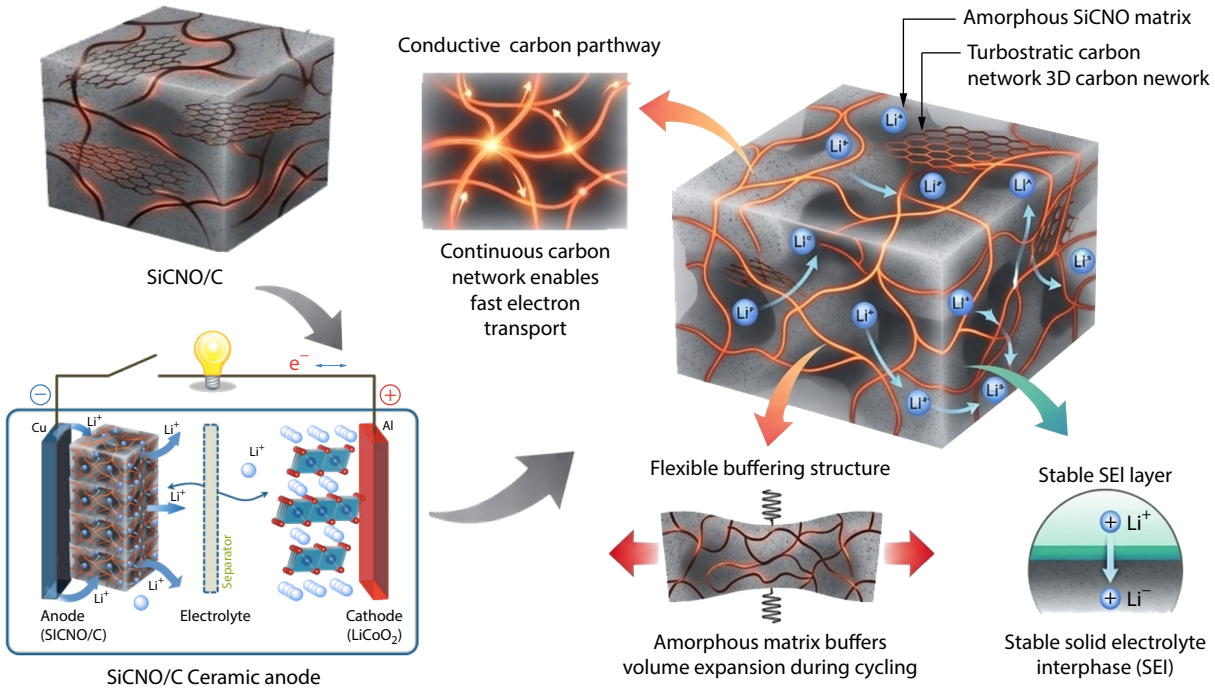

Fig. 8 Schematic illustration of the synergistic effect between the SiCNO ceramic matrix and the conductive carbon network, highlighting enhanced electron transport, buffered volume change, and improved lithium-ion diffusion in the SiCNO/C anode.

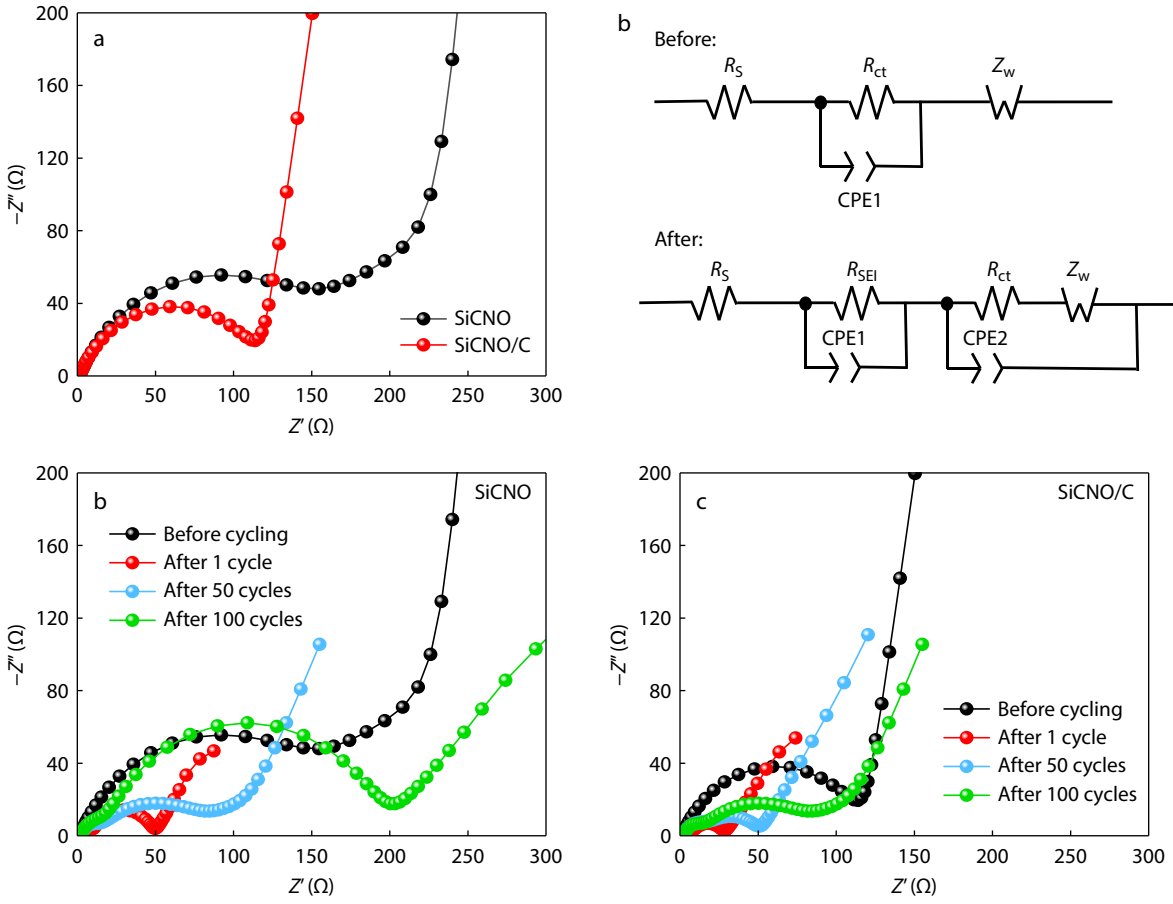

Fig. 9 (a) Nyquist diagram of SiCNO/C and SiCNO electrode before cycling; (b) Equivalent circuit diagram before and after cycling; Nyquist plots of (c) SiCNO and (d) SiCNO/C electrodes before and after cycling.

$cm^2 \cdot s^{-1}$), indicating accelerated lithium-ion diffusion kinetics. This enhancement originates from the synergistic effect of the PAN-derived carbon network, which not only improves the electronic conductivity, but also provides interconnected pathways for ion transport. Consequently, the SiCNO/C composite exhibited reduced polarization, faster reaction kinetics, and improved electrochemical stability.

Fig. 10 presents cross-sectional SEM images of the electrodes before and after cycling, with panels (a, b) corresponding to SiCNO and panels (c, d) to SiCNO/C after 100 cycles. Both electrodes exhibited noticeable thickness increases owing to the volume expansion during lithiation. Specifically, the thickness of the SiCNO electrode increases significantly from 28.9 μm to 79.4 μm, whereas the SiCNO/C electrode shows a much smaller change from 25.4 μm to 40.4 μm. The substantially suppressed expansion of SiCNO/C provided direct evidence of its enhanced structural stability. This improvement originates from the homogeneous incorporation of PAN-derived carbon within the SiCNO matrix, which forms a continuous conductive network. Such a carbon framework not only imparts mechanical flexibility to accommodate volume fluctuations during repeated lithiation/delithiation but also maintains electrode integrity by preventing particle pulverization and interfacial delamination. As a result, the SiCNO/C electrode preserved its structural coherence during cycling, which is critical for sustaining a stable electrochemical performance and long-term cycling durability.

To elucidate the lithiation mechanism of the SiCNO/C anode material, XRD and XPS analyses were performed on the working electrode before and after the cycling. The XRD results in Fig. S10(a) (in ESI) reveal three new diffraction peaks after cycling at 2θ angles of approximately 21°, 38°, and 45°. The peak at 38° corresponds to the formation of a silicon-lithium alloy phase, while the peak at 45° indicates the generation of lithium nitride (Li_3N), suggesting that a nitridation reaction occurs during lithiation. The peak at approximately 43° is attributed to amorphous carbon, and its increased intensity after cycling implies lithium-ion intercalation into the free-carbon phase. Additionally, the broad Si—O peak centered around 23° before cycling shifted slightly to 21° after cycling, implying the formation of an O—Si—O structure during lithiation.[35,36] Fig. S10(b) (in ESI) shows the XPS spectrum of Si 2p after lithiation, where the binding energy of Si decreases from 103.1 eV to 101.8 eV, indicating an alloying reaction between Si and Li.[37] In summary, the lithiation mechanism of the SiCNO/C anode involves a synergistic interplay of alloying reactions, carbon layer intercalation, and lithium adsorption at defect sites and nitrogen-doped sites. This multimode storage mechanism endows the material with excellent structural stability and superior kinetic performance.

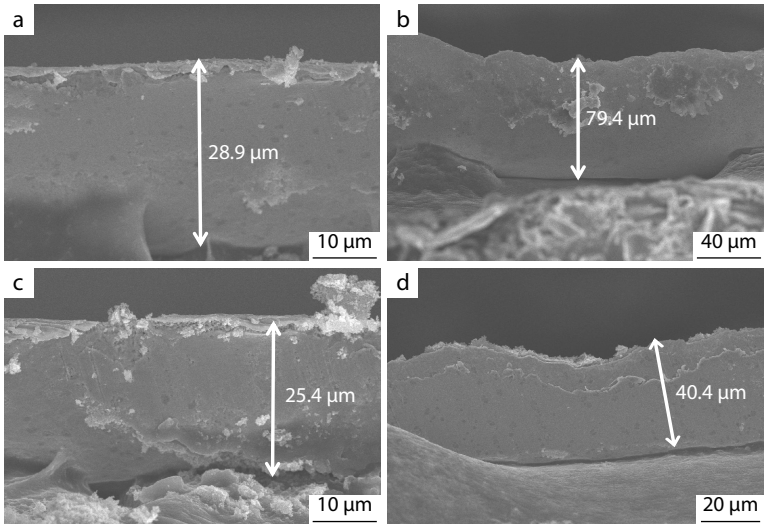

Fig. 10 Corresponding cross-sectional SEM images of the electrode before and after cycling: (a, b) for SiCNO after 100 cycles, and (c, d) for SiCNO/C after 100 cycles.

CONCLUSIONS

In this study, a novel polysilazane-acrylonitrile (PSZ/PAN) composite precursor was rationally designed to construct high-performance SiCNO/C anodes *via* high-temperature pyrolysis. The combination of radical polymerization and *in situ* acrylonitrile incorporation enabled molecular-level interpenetration between the polysilazane network and PAN segments, effectively suppressing phase separation and establishing a robust structural framework.

The derived SiCNO/C composite integrates the advantages of both components: the SiCNO ceramic matrix provides mechanical robustness to buffer volume variations, whereas the PAN-derived carbon forms a continuous conductive network that enhances electron transport and introduces abundant active sites. As a result, the SiCNO/C electrode delivers a high initial discharge capacity of 2749.0 mAh·g^{-1}, retains 1091.6 mAh·g^{-1} after 100 cycles at 100 mA·g^{-1}, and maintains 1050.1 mAh·g^{-1} after 600 cycles at 500 mA·g^{-1}. Moreover, the low volume expansion of 60.0% confirmed its superior structural stability during cycling.

These results highlight that molecular-level structural engineering of polymer-derived ceramics is an effective strategy for simultaneously achieving high capacity, enhanced conductivity, and long-term stability, offering promising prospects for advanced lithium-ion battery anodes.

Conflict of Interests

The authors declare no interest conflict.

Electronic Supplementary Information

Electronic supplementary information (ESI) is available free of charge in the online version of this article at http://doi.org/10.1007/s10118-026-3742-2.

Data Availability Statement

The data that support the findings of this study are available from the corresponding author upon reasonable request.

ACKNOWLEDGMENTS

This work was financially supported by the National Natural Science Foundation of China (No. 52572107), Natural Science Foundation of Chongqing, China (No. CSTB2025NSCQ-LZX0161), Shandong Provincial Natural Science Foundation Magnitude Fundamental Research, China (No. ZR2022ZD11), the Natural Science Foundation of Shandong Province (No. ZR2023ME003), and the Doctoral Fund of Qingdao University of Science and Technology (No. 12030430010828).

REFERENCES

1 Liu, H.; Zhao, L.; Ye, Y.; Yang, X.; Zhang, Y.; Li, Q.; Li, R.; Liu, H.; Huang, B.; Wu, F.; Chen, R.; Li, L. Extremely fast-charging batteries: principle, strategies, detection, and prediction. *Chem. Rev.* **2025**, *125*, 9553–9678.
2 Hu, Y.; Chen, Z.; Wang, Y.; Hou, H.; Chen, B.; Mitlin, D.; Liu, W. Review of thin lithium metal battery anode fabrication-microstructure-electrochemistry relations. *Adv. Mater.* **2025**, *38*, e11817.
3 Sun, L.; Liu, Y.; Wu, J.; Shao, R.; Jiang, R.; Tie, Z.; Jin, Z. A Review on recent advances for boosting initial coulombic efficiency of silicon anodic lithium ion batteries. *Small* **2022**, *18*, 2102894.
4 Dong, H.; Yang, T.; Liu, C.; Luo, D.; Liu, N.; Gao, Y.; Shi, Z.; Zhang, Y.; Chen, Z. Controllable and scalable prelithiation of dry silicon-based anodes for high-energy-density lithium-ion batteries. *Energy Storage Mater.* **2025**, *75*, 104072.
5 Xiao, J.; Sun, J.; Song, W.; Zhang, X.; Li, X.; Xie, H.; Lu, Z.; Fujishige, M.; Endo, M.; Niu, J.; Wang, F. Fast-charging graphite-based anode enabled by gradient silicon: from mechanism revelation to electrode design. *Energy Storage Mater.* **2025**, *78*, 104280.
6 Shang, C.; Li, X.; Wei, R.; Liu, X.; Xu, S.; Zhang, J. Research progress of metal oxide glass anode materials for lithium-ion batteries: a Review. *J. Non-Cryst. Solids* **2023**, *618*, 122547.

Graphical Abstract

Polyacrylonitrile (PAN)-derived Carbon Modification of Polysilazane Composite SiCNO/C as a High-performance Anode Material for Lithium-ion Batteries

Yi-Han Li, Yi-Wen Zhang, Jun-Hong Liu, Wen-Ze Xiao, Wen-Han Zang, Jing-Jiang Sun, Jian-Jiang He, Qing-Fu Wang, and Wei Zhao

Qingdao University of Science and Technology

Organic polysilazane (PSZ) and polyacrylonitrile (PAN) form a molecular interpenetrating network, yielding a polymer-derived SiCNO/C hybrid anode with high capacity, excellent cycling stability, and robust structure.

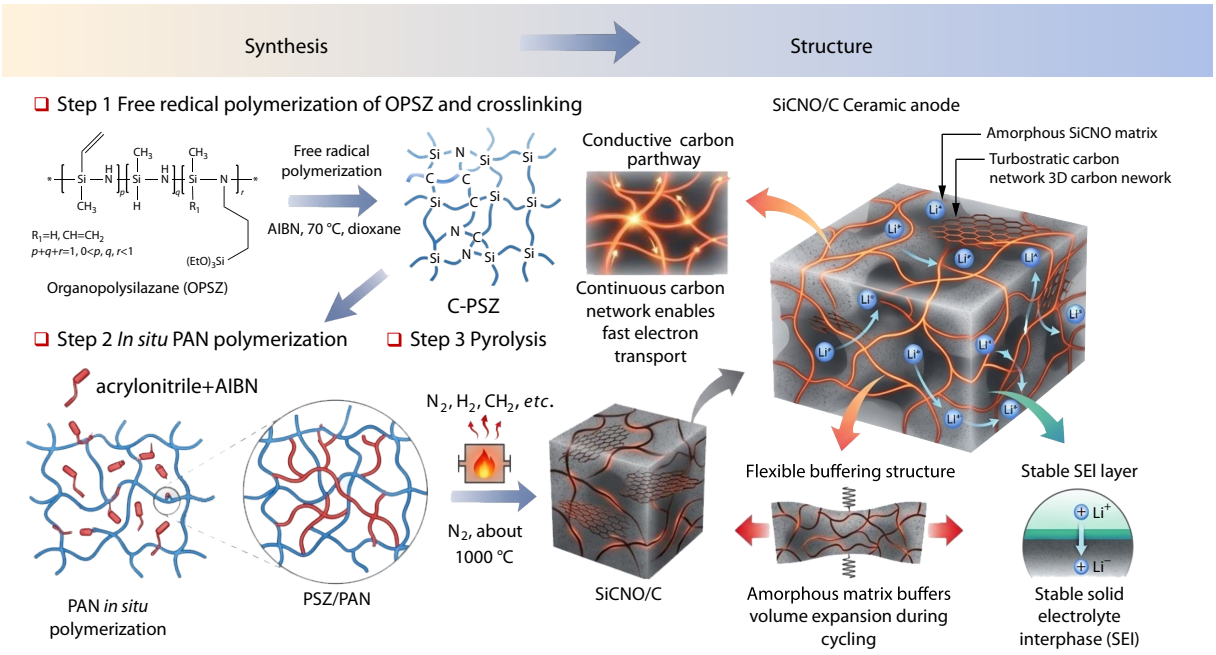

Chinese J. Polym. Sci., 2026 *https://doi.org/10.1007/s10118-026-3742-2*

7 Ren, W.; Zhou, Y.; Li, J.; Huang, L.; Sun, S. Si anode for next-generation lithium-ion battery. *Curr. Opin. Electrochem.* **2019**, *18*, 46–54.
8 Wang, L.; Zhang, H.; Song, Z.; Wang, H.; Lan, Y.; Yin, Z.; Yang, L.; Pan, F. Multidentate coordination chemistry enables adaptive ionic cross-linking of conductive binder for reversible silicon anodes. *J. Am. Chem. Soc.* **2026**, *148*, 7919–7930.
9 Hossain, M.; Hannan, M.; Ker, P.; Tiong, S.; Salam, M.; Abdillah, M.; Mahlia, T. Silicon-based nanosphere anodes for lithium-ion batteries: features, progress, effectiveness, challenges, and prospects. *J. Energy Storage* **2024**, *99*, 113371.
10 Cheng, Z.; Lin, H.; Liu, Y.; Li, J.; Jiang, H.; Zhang, H. Enabling the transport dynamics and interfacial stability of porous Si anode *via* rigid and flexible carbon encapsulation for high-energy lithium storage. *Small* **2024**, *20*, 2407560.
11 Lu, Z.; Zhao, Y.; Xu, D.; Hua, Z.; Chen, J.; He, X.; Zhang, X.; Zhang, J.; Shi, J.; Wen, R.; Li, G.; Guo, Y.; Wan, L. Constructing functional lithium-ion transport interfaces by in-situ growth and transformation on chemical vapor deposition-derived silicon-carbon anode materials. *J. Am. Chem. Soc.* **2026**, *148*, 9103–9113.
12 Wu, P.; Zheng, Z.; Shi, B.; Liu, C.; Chen, S.; Xu, B.; Liu, A. SiOC phase control and carbon nanoribbon growth by introducing oxygen at atom level for lithium-ion batteries. *Small Methods* **2022**, *6*, 2201299.
13 Zhang, L.; Fei, H.; Wang, C.; Ma, H.; Li, X.; Gao, P.; Wen, Q.; Tao, S.; Xiong, X. Silicon-based polymer-derived ceramics as anode materials in lithium-ion batteries. *Materials* **2025**, *18*, 3648.
14 Xia, X.; Zhang, Z.; He, J.; Wang, D.; Zhao, W.; Wang, Q. Synthesis of organopolysilazane nanoparticles as lithium-ion battery anodes with superior electrochemical performance *via* the two-step stober method. *ACS Appl. Mater. Interfaces* **2024**, *16*, 19507–19518.
15 Wang, D.; Xia, X.; Li, Y.; Sun, J.; He, J.; Wang, Q.; Zhao, W. Monodisperse and homogeneous SiCNO/C microspheres: A promising high-capacity and durable anode material for lithium-ion batteries. *Appl. Surf. Sci.* **2025**, *690*, 162574.
16 Zhang, Z.; Calderon, J.; Fahad, S.; Ju, L.; Antony, D.; Yang, Y.; Kushima, A.; Zhai, L. Polymer-derived ceramic nanoparticle/edge-functionalized graphene oxide composites for lithium-ion storage. *ACS Appl. Mater. Interfaces* **2021**, *13*, 9794–9803.

17 Graczyk-Zajac, M.; Fasel, C.; Riedel, R. Polymer-derived-SiCN ceramic/graphite composite as anode material with enhanced rate capability for lithium ion batteries. *J. Power Sources* **2011**, *196*, 6412–6418.
18 Pan, Y.; Cheng, C.; Chen, Y.; He, J.; Zhu, Z.; Wang, H. A new process for the carbonization of centrifugal electrospun polyacrylonitrile nanofibers driven by rapid joule heating. *J. Appl. Polym. Sci.* **2025**, *142*, e57733.
19 Ionescu, E.; Kleebe, H.; Riedel, R. Silicon-containing polymer-derived ceramic nanocomposites (PDC-NCs): preparative approaches and properties. *Chem. Soc. Rev.* **2012**, *41*, 5032–5052.
20 Ribeiro, L.; Flores, O.; Furtat, P.; Gervais, C.; Kempe, R.; Machado, R.; Motz, G. A novel PAN/silazane hybrid polymer for processing of carbon-based fibres with extraordinary oxidation resistance. *J. Mater. Chem. A* **2017**, *5*, 720–729.
21 Zhang, J.; Zhang, L.; Li, M.; Wan, X.; Fan, N.; Bai, M.; Shen, X.; Li, H. Synchronously enhanced multifunctional properties of carbon fiber/phenolic composites by constructing SiCN@PyC-CNTs heterointerface. *Ceram. Int.* **2025**, *51*, 65929–65938.
22 Chen, J.; Mao, Z.; Zhang, L.; Wang, D.; Xu, R.; Bie, L.; Fahlman, B. Nitrogen-deficient graphitic carbon nitride with enhanced performance for lithium ion battery anodes. *Acs Nano* **2017**, *11*, 12650–12657.
23 Hu, C.; Cen, Z.; Quan, Y.; Zhang, Q.; Jian, X.; Liang, K.; Song, Y.; Xu, J. SiOC/CNTs composites as anodes for lithium-ion batteries. *Chem. Eng. J.* **2024**, *493*, 152610.
24 Hsu, C. H.; Chen, H. Y.; Tsai, C. J. Stoichiometry dependence of electrochemical behavior of silicon oxide thin film for lithium ion batteries. *J. Power Sources* **2019**, *438*, 226943.
25 Huang, W.; Gao, J.; Miao, L.; Zhou, J.; Yang, G.; Liu, W.; Jiang, Y.; Qin, H.; Zhang, Z.; Lei, X.; Lu, A.; Mo, Z.; Zhang, D.; Dang, F. Si@nitrogen-doped carbon nanoparticles for lithium-ion battery anodes. *ACS Appl. Nano Mater.* **2024**, *7*, 10350–10360.
26 Lee, S. J.; Lee, J. K.; Chung, S. H.; Lee, H. Y.; Lee, S. M.; Baik, H. K. Stress effect on cycle properties of the silicon thin-film anode. *J. Power Sources* **2001**, *97*, 191–193.
27 Berg, C. M.; Morasch, R.; Gasteiger, H. A. Silicon hysteresis and voltage relaxation phenomena: Implications on the characterization of anode overpotentials. *J. Electrochem. Soc.* **2025**, *172*, 050516.
28 Luo, Y.; Yang, D.; Chen, Z.; Wang, L.; Xu, B.; Zhou, G.; Liu, W. Stress-dissipating cocontinuous carbon-silicon microparticles for high-energy lithium-ion batteries with low expansions. *Nano Lett.* **2025**, *25*, 15231–15239.
29 Yang, D.; Chen, M.; Han, R.; Luo, Y.; Li, H.; Kang, Z.; Chen, Y.; Fu, J.; Iqbal, N.; Liu, W. Sealing porous carbon *via* surface-initiated polymerization achieves low-surface-area Si-C microparticles for Li-ion batteries. *Nano Energy* **2024**, *127*, 109744.
30 Miao, J.; Zhang, J.; Liu, Y.; Ma, W.; Ding, Y.; Cui, S. Dual-functional SiOC: Achieving record 86% initial Coulombic efficiency in Li-ion batteries and dendrite-free Li metal anodes *via* (110)-textured deposition. *Nano Res.* **2026**, *19*, 94908284.
31 Arca, E.; Veith, G.; Satish, R.; Lin, T.; Teeter, G.; Kostecki, R. Understanding the origin of the nonpassivating behavior of Si-based anodes during the Initial cycles. *J. Phys. Chem. C* **2022**, *126*, 14058–14066.
32 Hu, Z.; Bian, L.; Li, H.; Zhang, X.; Gao, J.; Tian, R.; Xing, L.; An, S. Enhanced lithium-ion storage of silicon-carbon composite by homogeneous carbon coating and pore regulation for lithium-ion batteries. *Ceram. Int.* **2025**, *51*, 32522–32529.
33 Wang, D.; Kong, L.; Zhang, F.; Liu, A.; Huang, H.; Liu, Y.; Shi, Z. Porous carbon-coated silicon composites for high performance lithium-ion batterie anode. *Appl. Surf. Sci.* **2024**, *661*, 160076.
34 Yin, L.; Park, M.; Jeon, I.; Hwang, J.; Kim, J.; Lee, H.; Park, M.; Jeong, S.; Cho, C. Silicon nanoparticle self-incorporated in hollow nitrogen-doped carbon microspheres for lithium-ion battery anodes. *Electrochim. Acta* **2021**, *368*, 137630.
35 Misra, S.; Liu, N.; Nelson, J.; Hong, S. S.; Toney, M. F. *In situ* X-ray diffraction studies of (de)lithiation mechanism in silicon nanowire anodes. *Acs Nano* **2012,** *6*, 5465.
36 Sun, Y.; Li, Y.; Sun, J.; Li, Y.; Pei, A.; Cui, Y. Stabilized Li3N for efficient battery cathode prelithiation. *Energy Storage Mater.* **2017**, *6*, 119–124.
37 Huo, H.; Jiang, M.; Bai, Y.; Ahmed, S.; Volz, K.; Hartmann, H.; Henss, A.; Singh, C. V.; Raabe, D.; Janek, J. Chemo-mechanical failure mechanisms of the silicon anode in solid-state batteries. *Nat. Mater.* **2024**, *23*, 543–551.

https://doi.org/10.1007/s10118-026-3742-2